Results in Engineering 24 (2024) 103109

Contents lists available at ScienceDirect

Results in Engineering

journal homepage: www.sciencedirect.com/journal/results-in-engineering

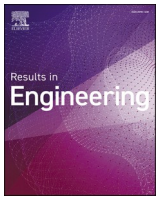

A facile approach for fabricating g-C_3N_4-based materials as metal-free photocatalysts

Monika Michalska [a,*], Jiri Pavlovsky [a], Eva Scholtzova [b,**], Peter Skorna [b], Vlastimil Matejka [a], Kamil Bochenek [c], Amrita Jain [c], Koki Chida [d], Takeharu Yoshii [d], Hirotomo Nishihara [d,e]

[a] Department of Chemistry and Physico-Chemical Processes, Faculty of Materials Science and Technology, VSB-Technical University of Ostrava, 17. listopadu 2172/15, 708 00, Ostrava-Poruba, Czech Republic
[b] Institute of Inorganic Chemistry of Slovak Academy of Sciences, Dúbravská cesta 9, Bratislava, 84536, Slovakia
[c] Institute of Fundamental Technological Research, Polish Academy of Sciences, Pawińskiego 5B, 02-106, Warsaw, Poland
[d] Institute of Multidisciplinary Research for Advanced Materials, Tohoku University, 2-1-1 Katahira, Aoba-ku, Sendai, 980-8577, Japan
[e] Advanced Institute for Materials Research (WPI-AIMR), Tohoku University, 2-1-1 Katahira, Aoba-ku, Sendai, 980-8577, Japan

ARTICLE INFO

Keywords:
Melem
g-C_3N_4
Acid orange 7
Photocatalytic degradation
DFT-D3
Modeling

ABSTRACT

This study presents a novel, straightforward approach for synthesizing graphitic carbon nitrides (g-C_3N_4, g-CN) from melamine, requiring merely 30 min of thermal holding at temperatures ranging from 400 to 550 °C in an atmosphere comprising either nitrogen or air. Elemental analysis, X-ray powder diffraction (XRD), Fourier-transform infrared spectroscopy (FTIR), diffuse reflectance (UV–Vis DRS), photoluminescence (PL) spectroscopy and scanning electron microscopy (SEM) were employed to assess the quality of the as-prepared powders. Furthermore, theoretical calculations utilizing the Density Functional Theory (DFT) method were conducted to reinforce the experimental findings of the research. A further investigation of the thermal stability of the selected sample was conducted using a unique combination of thermogravimetry–coupled with differential scanning calorimetry, quadrupole mass spectrometry (TG-DSC-MS) and advanced temperature-programmed desorption (TPD) analyzes. The current study focuses on the effect of synthesis conditions (temperature and nitrogen/air environment) on the structure, morphology, and photocatalytic performance of g-C_3N_4 compounds synthesized using this approach. The g-C_3N_4-based materials were examined as potential photocatalysts using the acid orange 7 (AO7) photodegradation methodology. To enable comparison of the photodegradation experiments, two separate lamps with wavelengths of 360 nm (UV light) and 420 nm (VIS light) were utilized. The primary objective was to present a novel method for the synthesis of g-C_3N_4-based materials. This was achieved by demonstrating that organic composites generated at lower temperatures have the best photocatalytic capabilities. Furthermore, the approach to achieving high-quality photocatalysts was shown to be cost-effective, environmentally friendly, and scalable.

1. Introduction

Graphitic carbon nitride (g-C_3N_4, g-CN) is a two-dimensional (2D) metal-free polymeric material that has been the subject of extensive research in recent years due to its semiconducting characteristics [1–6]. Among its defining attributes are high thermal, physical, chemical, and photochemical stability. Because of its nontoxicity, low cost, and ease of fabrication, graphitic carbon nitride has a diverse range of applications in photocatalytic processes, including carbon dioxide capture and reduction [7], hydrogen production [8–11], and so on [12–17]. Due to its 2.70 eV bandgap energy (ca. 460 nm), it is capable of absorbing visible light, rendering it beneficial for a multitude of applications, including the construction of solar cells [18].

Thermal polymerization of precursors such as urea [19], thiourea [19,20], cyanamide, dicyandiamide [21], and melamine [21,22] can yield g-C_3N_4 [14,23]. Polycondensation and polyaddition are two processes that contribute to the formation of g-C_3N_4 and are temperature-dependent. Melamine is formed when the precursors undergo polymerization (polyaddition). The loss of ammonia causes melamine to condense (polycondensation), leading to the formation of the

* Corresponding author.
** Corresponding author.
E-mail addresses: monika.kinga.michalska@gmail.com (M. Michalska), eva.scholtzova@savba.sk (E. Scholtzova).

https://doi.org/10.1016/j.rineng.2024.103109
Received 25 July 2024; Received in revised form 20 September 2024; Accepted 10 October 2024
Available online 11 October 2024

g-C_3N_4 polymer through the melam (ca. 300 °C), melem (400–500 °C), or melon (up to 550 °C) structures [24,25]. At approximately 550 °C, melon polymerizes to form g-C_3N_4 planar structures. Among the various products, melem is the only one to exhibit superior thermodynamic stability, existing in a temperature range of 400–500 °C [24–26].

In general, grain size, pore volume, and surface area may affect the physicochemical properties of different materials, such as g-C_3N_4. A variety of physical and chemical methods have been employed to obtain g-C_3N_4 material, including sol-gel [27], hydrothermal [21,28,29], and solvothermal [30–32]. These methods are time-consuming, expensive, and require several stages to be completed, as well as the use of specific equipment. One cost-effective and scalable approach is the direct thermal polymerization approach, which can yield a higher amount of the assumed g-C_3N_4 product. Based on our previous works and experience, we demonstrated that melamine is the most effective of the possible precursors and meets the aforementioned sophisticated requirements [26].

Melamine (2,4,6-triamino-1,3,5-triazine) represents an important primary material for several industrial applications, including the synthesis of melamine-formaldehyde resins and fireproof materials with high surface hardness and good heat and flame resistance [33,34]. Furthermore, melamine is employed in the construction of supramolecular structures, such as those formed by cyanuric acid ($C_3N_3(OH)_3$) or melamine derivatives (e.g., melamine-formaldehyde resins) [35–37]. In various scientific groups engaged in the study of advanced carbon materials, there has been a growing interest in melamine and other compounds containing s-triazine (cyanuric) rings, such as cyanuric chloride $C_3N_3Cl_3$ [38–42] or cyanuric azide $C_3N_3(N_3)_3$ [43], which are considered suitable molecular precursor compounds for synthesizing graphitic forms of carbon nitride (g-C_3N_4) [44–46].

The methods of quantum mechanics have been successfully applied to the study of various types of carbon materials [47], as evidenced by the examination of the electronic structure of graphitic carbon nitride systems using the DFT approach [46]. The structural parameters, configuration, and bonding of the studied melamine [24,48], melam [24,48], melem [24,48], and polymeric melon and g-C_3N_4 [24,49,50] structures in the unit cell were obtained from theoretical calculations.

Tao et al. [51] prepared g-C_3N_4 by thermally decomposing 20 g of melamine powder. The powder was placed in a covered alumina crucible and heated to 500 °C for 1 h at a rate of 3 °C/min in a muffle furnace. Subsequently, the temperature was rapidly raised to 520 °C in 5 min and held for an additional hour. Once the furnace had cooled to room temperature, the sample was removed. The material achieved a photoactivity of 40 % after 30 min during the photodegradation test with AO7 under visible light [51]. Ganesan and co-authors [52] placed 10 g of melamine in an alumina crucible and heated it at a rate of 5 °C/min until it reached 550 °C. The temperature was then maintained at 550 °C for 4 h in static air, forming yellow-coloured materials. The material's photoactivity was found to be 24 % after a 60 min photodegradation test using methyl orange (MO) under UVA light with a wavelength of 365 nm [52]. In order to fabricate bulk g-CN, Praus et al. [53] employed a heating method in which melamine was directly heated at 550 °C for a period of 4 h at a heating rate of 3 °C/min in an atmosphere of nitrogen and air. Upon irradiation with visible light (420 nm), bulk g-CN powder heated in air demonstrated 15 % photoactivity, while in nitrogen, approximately 6 % photoactivity towards AO7 was observed after 60 min of irradiation [53]. Senthil et al. [54] reported that the photoactivity of AO7 (concentration of 5×10^{-5} M) for pure g-C_3N_4 reached almost 55 % after 60 min under a visible light source with a wavelength of 380–800 nm. The synthesis of g-C_3N_4 powder was conducted by the authors [54] using an inexpensive urea precursor loaded in an alumina crucible with a lid to prevent sublimation. The furnace was heated to 520 °C for 2 h at a heating ramp of 15 °C/min, after which the temperature was allowed to spontaneously cool to room temperature [54]. Ming et al. [55] yielded the g-C_3N_4 product through mechanical mixing by grinding 3.0 g melamine and 7.0 g thiourea. The mixture was heated at a rate of 2 °C/min for 4 h at 530 °C. The authors [55] achieved 20 % photoactivity over AO7 under visible light after 60 min. In our previous work [26], we synthesized a melem/g-C_3N_4 composite through direct thermal treatment of the melamine precursor in an air flow at 550 °C. The heating regime involved treating 10 g of melamine in a semi-closed alumina crucible with an alumina lid at a rate of 3 °C/min until it reached 550 °C. The crucible was immediately removed from the furnace once the temperature was reached. The composite of melem/g-C_3N_4 exhibited photodegradation activities of over 75 % and 41 % using a UV lamp (1 h, 368 nm) and a VIS lamp (1 h, 420 nm), respectively [26].

This work presents a novel and efficient synthesis approach to obtain graphitic carbon nitride (g-C_3N_4) compounds from melamine. This is achieved through a short 30-min thermal treatment at relatively low temperatures (400–550 °C) in either nitrogen or air. Although comparable synthesis routes have been previously investigated [51–55], our approach is distinguished by its emphasis on markedly reduced thermal treatment times and a comparison between the synthesis of materials in both nitrogen and air atmospheres. This provides new insights into the effects of these conditions on the properties and performance of the resulting materials.

The study focuses on a comprehensive investigation into the influence of temperature and atmospheric conditions on the structural, morphological, and photocatalytic characteristics of g-C_3N_4-based organic composites, with a particular focus on its ability to degrade the model dye acid orange 7 under ultraviolet (UV) and visible (VIS) light irradiation. It is noteworthy that the materials synthesized at lower temperatures were found to exhibit superior photocatalytic activity. This indicates the potential for a significant reduction in manufacturing time, energy consumption and costs, while still producing high-quality photocatalysts.

This work also includes a comprehensive comparative study, the first of its kind, between materials synthesized in nitrogen and air, and their photocatalytic efficiencies, which addresses a gap in the literature. Moreover, advanced characterization techniques, including thermogravimetry coupled with differential scanning calorimetry, quadrupole mass spectrometry (TG-DSC-MS), and temperature-programmed desorption (TPD), were employed to investigate the thermal stability and structural transformations of the synthesized materials, thereby adding a distinctive analytical dimension to our research. In addition, density functional theory (DFT) calculations were conducted to corroborate the experimental findings, thereby facilitating a more profound comprehension of the photocatalytic mechanisms at the atomic level. Furthermore, the roles of various photogenerated species (such as radicals and holes) in the degradation process were investigated using scavengers, thereby advancing our understanding of the photocatalytic pathways involved.

The present study is distinguished from previous research by its use of a synthesis method requiring minimal time, the involvement of both nitrogen and air atmospheres, and a focus on the creation of g-C_3N_4-based organic composites with enhanced photocatalytic activity. Moreover, the findings demonstrate that superior photocatalytic efficiency can be achieved without the incorporation of i.e. transition metal oxides (TMO) to create a TMO/g-C_3N_4 composite, a strategy frequently employed in other studies [11–13,15,17,54]. Ultimately, this research proposes a novel approach for developing g-C_3N_4-based materials that optimize both performance and cost-efficiency, advancing the limits of current synthetic methodologies.

2. Experimental details

2.1. Synthesis of g-C_3N_4-based materials

The series of g-C_3N_4 compounds were prepared by thermal treatment processing of the melamine (ME) precursor (4.2 g) in nitrogen or air atmosphere for 30 min at 400, 450, 500, and 550 °C, respectively. The

heating rate for all prepared materials was set to 5 °C/min. The ME was placed in highly pure alumina oxide crucibles. The series of ME-T-N/A (where T – temperature, N – nitrogen, or A – air atmosphere) samples were subjected to annealing at temperatures (T) of 400, 450, 500, and 550 °C, respectively. The samples labelled ME-400-N, ME-450-N, ME-500-N, and ME-550-N were synthesized in a tube furnace in a nitrogen atmosphere. In contrast, the samples labelled ME-400-A, ME-450-A, ME-500-A, and ME-550-A were heated by a muffle furnace in an air atmosphere.

Furthermore, in order to facilitate comparison between our materials, we undertook the synthesis of two samples at 520 and 550 °C in air. The details of the synthesis conditions and the examination results are presented and discussed in the Supplementary Material.

2.2. Instrumentation details

The carbon (C), nitrogen (N), and hydrogen (H) contents in the g-C_3N_4 compounds were determined using a CHSN 628 Series (LECO, Corp, St. Joseph, MI, USA) elemental analyzer. The oxygen content was calculated as a difference of 100 % organic content (excluding ash).

XRD analysis was performed on the X-ray diffractometer MiniFlex 600 (Rigaku, Japan), equipped with a Co tube operated at 40 kV and 15 mA. D/teX Ultra 250 was used as a detector. XRD patterns were collected at room temperature in the range of $6^\circ \leq 2\theta \leq 60^\circ$ using a step size of 0.01° and a scanning rate of 3°/min.

A thermal analysis of g-C_3N_4 was conducted using a thermogravimetry-differential scanning calorimetry (TG-DSC; STA 449 Jupiter, Netzsch) with a heating rate of 10 °C min^{-1} under a He flow (150 mL min^{-1}). The emission gas from TG-DSC was analyzed by a quadrupole mass spectrometer (MS; JMS-Q1500GC, JEOL). The thermal decomposition behavior of g-C_3N_4 was also analyzed by advanced temperature-programmed desorption (TPD) up to 1800 °C [47,56,57].

The Fourier transform infrared (FTIR) spectra of the prepared samples were measured using an FT/IR-6600 (JASCO, Japan). Measurements were carried out in the range of 500–4000 cm^{-1} with a resolution of 2 cm^{-1} using an attenuated total reflection (ATR) technique. Each spectrum obtained was the average of 64 scans. Prior to each measurement, the background was scanned to eliminate apparatus and environmental effects.

Reflectance data were obtained by measuring the UV–VIS spectra of dry powder samples at room temperature using a Shimadzu UV-2600 Series spectrophotometer equipped with an IRS-2600Plus integrating sphere (Shimadzu Ltd, Japan) in the wavelength range of 220–800 nm. The Kubelka-Munk function was applied to transform the data, and the values of the indirect bandgap energies (E_g) were determined using Tauc plot. A sample of powdered $BaSO_4$ was employed as a reference.

The photoluminescence (PL) emission spectra of all obtained g-C_3N_4-based materials were determined at room temperature, using an Edinburgh Instrument Ltd FLSP920 Series spectrometer in the wavelength range of 350–600 nm. The spectrometer was equipped with a 450 W non-ozone xenon lamp (Steady state Xe900 lamp) and an R928P detector (PMT detector). In this experiment, the Czerny-Turner arrangement was employed.

Microscopic investigations were performed using a scanning electron microscope (Zeiss Crossbeam 350). Prior to characterization, the samples were gold-sputtered to ensure optimal electron conductivity.

2.3. Photocatalytic activity measurements

The photocatalytic activity of the prepared samples was evaluated by subjecting them to photodegradation of acid orange 7 (AO7, 7.14 × 10^{-4} mol/L) photodegradation under UV (360 nm, irradiation intensity: I = 3.40 mW/cm^2) and VIS (420 nm, irradiation intensity: 10 mW/cm^2) light irradiation. In a typical procedure, 50 mg of the catalyst (ME-T-N/A) was dispersed in 150 mL of deionized water and magnetically stirred at 300 rpm at room temperature to obtain a homogeneously dispersed suspension. After that, a 15 mL AO7 solution was added to the suspension. The concentration of AO7 for each photodegradation measurement was 25 mg/L [26]. All as-prepared suspensions were magnetically stirred at 300 rpm for 30 min at room temperature in the dark to estimate the adsorption equilibrium of AO7 dye on the given sample. Subsequently, the UV or VIS lamp was switched on. After the dark period and within a given time of the irradiation period, 2 mL of a homogeneously dispersed suspension was sampled using a syringe. The suspensions were filtered using a 0.45 mm pore size syringe filter (CHROMAFIL GF/RC-20/25 filters, Macherey-Nagel, Germany) directly into the 1 cm quartz glass microcuvette in order to separate the photocatalytic material. The absorbances of the obtained filtrates were recorded at 480 nm using Helios Epsilon (ThermoFisher, USA) spectrometer. The extent of AO7 degradation (A_{sample}) was calculated for all studied samples, according to the equation: $A_{sample} = (1-(C_{eq.\ AO7}/C_{0\ AO7}))$ x 100 %, where $C_{eq.\ AO7}$ is the concentration of AO7 at a given time of irradiation, and $C_{0\ AO7}$ is the initial concentration of AO7 [26].

The photodegradation tests were further carried out in the presence of ethylenediaminetetraacetic acid (EDTA) (1 mmol/L), 1,4-benzoquinone (1,4-BQ) (1 mmol/L) and t-butanol (t-Bu) (1 mmol/L) as the scavengers of the holes (h^+), the superoxide radicals ($\bullet O_2^-$) and hydroxyl radicals (•OH) [26,58–60]. For the experiments, suspensions of 36 mg of the ME-T-N/A sample were prepared with 20 mL of the scavenger, 88 mL of demineralised water, and 12 mL of AO7 (20 mg/L). All ME-T-N/A samples were subjected to photodegradation experiments under UV and VIS light irradiation. Each experiment consisted of a 1-h dark period and a 2-h long irradiation period. The extent of the AO7 photodegradation after the 1-h long dark and 2-h long irradiation period was obtained using the same procedure as previously described for the photodegradation test without scavengers [26].

3. Computational details

3.1. Computational methods

All studied structural models, melamine, melam, melem, melon and g-C_3N_4, were examined using the density functional theory (DFT) method implemented in the Vienna *Ab initio* Simulation Package (VASP) [61,62]. The exchange-correlation energy was described by Perdew, Burke, and Ernzerhof (PBE) functional [63] based on the generalized gradient approximation (GGA) theory. The Kohn-Sham equations were calculated using the variation method with a plane-wave (PW) basis set with the kinetic energy cut-off of 500 eV in the projector-augmented-wave (PAW) method [64,65]. For the integration over the Brillouin Zone, a Monkhorst-Pack 2 × 2 × 2 *k*-point mesh was used. The atomic positions and the unit cell parameters were fully optimized (Fig. S1, Table S1). No symmetry restrictions were applied during any optimization procedure. The relaxation criteria were 10^{-5} eV/atom for the total energy change and 0.015 eV/Å for the maximally allowed forces acting on each atom. Due to the presence of weak interactions between the molecules in the unit cell, DFT calculations were performed using the D3 scheme to correct dispersion forces acting in the structure [66]. The DFT-D3 method was applied to periodic structural models to obtain calculated powder diffraction spectra.

The calculations of theoretical UV/Vis spectra of respective structures of reactants were done using cluster models (melam, melem, melon and g-C_3N_4) by means of the Gaussian 16 program package [67] employing the DFT method and B3LYP [68] functional without any constraints. The energy cut-off for geometry optimizations was 3 × 10^{-3} kJ mol^{-1}, and the final root mean square energy gradient was below 1.5 kJ $mol^{-1}Å^{-1}$. The geometry optimizations were performed in a large 6–311++G** basis set [69]. The real minima of the optimized structures were confirmed by frequency calculations (no imaginary frequency). For the calculation of the excited states of studied systems and, subsequently, preparation of the calculated UV/Vis spectra, the time-dependent density functional theory (TD-DFT) [70] method with

the B3LYP functional and 6–311++G** basis set was used.

3.2. Computational models

The optimized models based on the real crystal structures of melamine, melam, melem and polymeric systems of melon and g-C_3N_4 are presented in Fig. S1. The optimized unit cell parameters of all investigated periodic models are summarised in Table S1 and are in good agreement with experimental structural parameters. The melamine elementary cell [71] consists of four melamine molecules in two differently-oriented layers in the unit cell. The melamine molecule is defined as a trimer of cyanamide with a 1,3,5-triazine skeleton (Fig. S1a). It is a monoclinic crystallographic structure in $P2_1/a$ space group of symmetry with nearly planar triazine rings. The elementary cell of the melam structure [72] is monoclinic in a $C2/c$ space group of symmetry consisting of 14 molecules. The structure of melam molecules is characterized by two triazine units condensing through a bridging NH group (Fig. S1b). The monoclinic melem [25] crystal structure with the space group $P2_1/c$ consists of four 2,5,8-triamino-heptazine molecules in the unit cell interconnected by extended hydrogen bridges. Two differently-oriented layers of parallel molecules alternate along the direction of the *c*-axis. Each molecule contains a cyameluric nucleus C_6N_7 of three *s*-triazine rings. The structure is completed by three terminal N atoms bound to positions 2, 5, and 8 of the tri-s-triazine C_6N_7 nucleus (Fig. S1c). A polymer structure characterizes melon and g-C_3N_4 models (Figs. S1d and e) [73]. Melon contains the cyameluric nucleus C_6N_7 in the crystal structure. It comprises layers made up of infinite chains of NH-bridged melem monomers. On the other hand, g-C_3N_4, as a final product of the reaction, is created by heptazine rings cross-linked by tertiary N atoms forming extended 2D sheets.

The melam, melem, melon and g-C_3N_4 cluster models shown in Fig. S2 were used to calculate UV/Vis spectra and compare them with experimental UV/Vis measurements in the temperature range between 400 and 550 °C. Mutual comparison can confirm/decline the presence of respective reactants in the experimentally measured probes.

4. Results and discussion

4.1. Elemental analysis

Elemental analysis was used to find the C, N, and H content in the ME-T-N/A samples. The results are included in Table 1. The findings are presented in Table 1. Furthermore, the experimental outcomes were contrasted with the theoretical simulations, and, in accordance with the chemical formula, the structure was elucidated in Table S2.

The C/N molar ratio of 0.61 obtained for the sample heated at 400 °C is close to the theoretical ratios of 0.60 and 0.54 attributed to melem [74] and remaining melam [74], respectively. With an increase in heating temperature by 50 °C, melem was formed, and the experimental and theoretical C/N molar ratios [74] were almost equal. At a temperature of 500 °C (with an experimental C/N molar ratio of 0.65), the melon structure (with a theoretical C/N molar ratio of 0.67 [75]) was predominant with some remaining melem (with a theoretical C/N molar ratio of 0.60 [74]). Upon annealing melamine at 550 °C, the g-C_3N_4 structure predominated with the remaining melon content. It is apparent that the estimated experimental results are in line with the theoretical values [75]. Furthermore, the achieved C/N molar ratios in nitrogen or air atmosphere at the same temperatures were comparable. Later, the results were supported by XRD and DFT modeling as well. It is also noteworthy that the hydrogen content of the samples heated in a nitrogen atmosphere is higher than in the air atmosphere, while the oxygen content is lower in the samples heated in nitrogen than in the air atmosphere.

Table 1
Elemental analysis of C, N, and H contents of ME samples after thermal treatment at 400, 450, 500, and 550 °C in nitrogen (series **N**) and air (series **A**) atmosphere.

Material	C	N	H	O[a]	N/C
	(wt%/mol.%)				C/N
ME-400-N	32.9/23.9	63.0/39.1	4.27/37.0	0.00/0.000	1.91/1.64 0.52/0.61
ME-450-N	33.4/26.1	62.9/42.0	3.40/31.7	0.30/0.176	1.88/1.61 0.53/0.62
ME-500-N	34.0/25.9	61.3/39.9	3.69/33.5	1.01/0.578	1.80/1.54 0.55/0.65
ME-550-N	35.2/29.5	61.6/44.1	2.61/26.1	0.59/0.371	1.75/1.50 0.57/0.67
ME-400-A	33.0/27.6	63.2/45.1	2.68/26.7	1.12/0.702	1.92/1.64 0.52/0.61
ME-450-A	33.2/26.1	62.7/422	3.33/31.2	0.77/0.455	1.89/1.62 0.53/0.62
ME-500-A	33.9/28.5	61.0/43.7	2.62/26.2	2.48/1.564	1.80/1.54 0.56/0.65
ME-550-A	34.9/31.8	61.3/47.7	1.75/19.0	2.05/1.404	1.76/1.51 0.57/0.67

[a] The content of oxygen was calculated as a difference of 100 % organic content (excluding ash).

4.2. X-ray powder diffraction analysis

X-ray powder diffraction analysis was used to track changes in the phase and structure of the materials under investigation, and the results are included in Fig. 1. A slight difference was observed between the intensities of samples heated in nitrogen and air atmospheres. The XRD analysis, supported by calculated (DFT-D3) theoretical models (Fig. 2), helped to identify the dominant and predominant phases presented in Fig. 3. These were then compared with the results of the elemental analysis (discussed above). In summary, the XRD patterns for the samples heated at 400 °C were attributed to melem [25,48,74] as a dominant phase and remaining melam [25,48,74], respectively. It was observed that a pristine melem structure was created when the heating temperature was raised by 50 °C [24–26,48,74]. At 500 °C, the melon structure [24.25, 50, 75] is the predominant phase, with some remaining melem [24–26,48]. The g-C_3N_4 structure [75,76] was found to be dominated by a remaining melon [50,75] content following annealing melamine at 550 °C.

The achieved patterns agree well with the calculated results obtained by the DFT-D3 method (Figs. 2 and 3).

All studied compounds exhibited well-distinguishable reflection patterns indicative of distinct crystallographic phases. The calculated highly intensive peaks at 28.83° for g-C_3N_4 and 32.20° of 2θ for melem crystal are well-known in discotic systems as the stacking peak of conjugated aromatic rings (Fig. 2) [49]. The crystal structure of melem exhibits a very intense reflection at 14.34°, which corresponds to the plane arrangement of the nitrogen-bonded heptazine units. In the same XRD area, a low-intensity reflection was also observed in the structure of melon crystal (14.71°) [49]. The calculated and experimentally obtained XRD patterns clearly indicate that increasing temperature results in a decrease in the number and intensity of peaks up to 550 °C. At this temperature a typical reflection of g-C_3N_4 at 28.78° (calculated, DFT-D3) and at 31.80° of 2θ (experiment) was observed.

The calculated XRD data and experimental measurements were found to be in good agreement with the results obtained in the literature. Yuan et al. [48] conducted a study of the XRD of melam and melem crystal structure using theoretical DFT calculations in the Reflex package of the Materials Studio program and experimental techniques. Furthermore, Lau et al. [77] focused on the experimental XRD study of crystalline melem, oligomers of melem and melon with the objective of controlling the polymerization process for the formation of graphitic carbon nitride polymer structures, which exhibited a substantially enhanced photocatalytic activity. In a separate study, Tyborski et al. [73] employed both experimental and theoretical approaches to

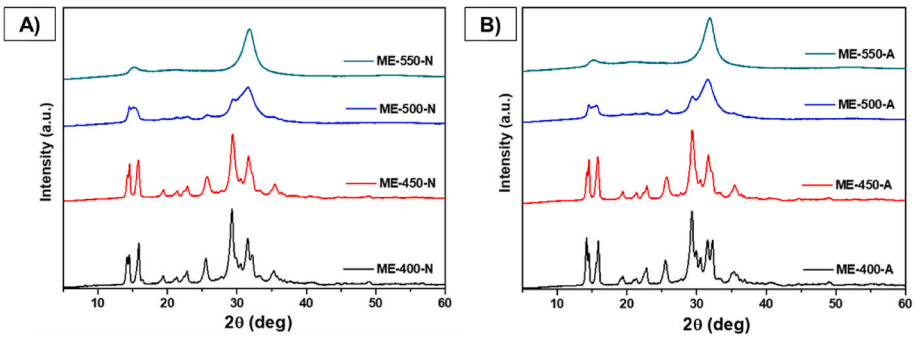

Fig. 1. XRD patterns of ME samples after thermal treatment at 400, 450, 500, and 550 °C in nitrogen (**A**) and air (**B**) atmosphere.

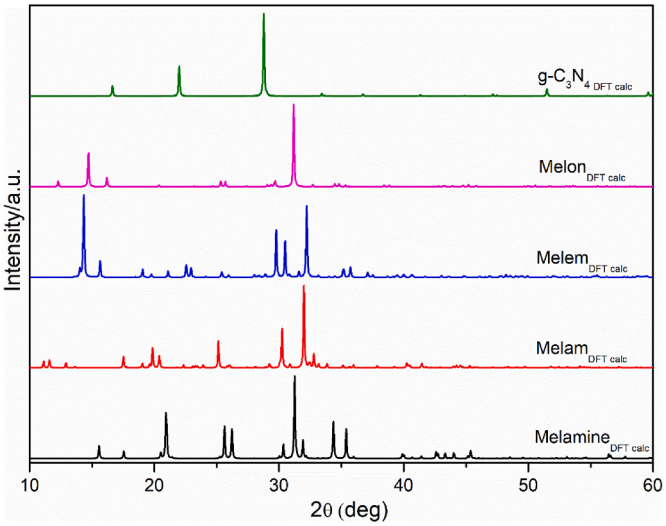

Fig. 2. Calculated XRD patterns of the respective structures using DFT-D3 method.

investigate the XRD of polymeric graphitic carbon nitride. Their theoretical diffraction pattern encompassed all significant features observed in X-ray diffraction. These analyses were conducted using the Diamond 3.2i program, with results reviewed using the PowderCell 2.4 program.

4.3. Thermal analysis

The transformation from melamine to melam/melem composite (400 °C), through pristine melem (450 °C), melem/melon composite (500 °C), and finally to melon/g-C_3N_4 (550 °C) was found to be in exact accordance with the results presented in Table 1. The thermal stability of ME-550-N was further investigated using TG-DSC-MS (Fig. S3) and TPD (Fig. S4). ME-550-N shows a small weight loss (ca. 1 wt%) below 300 °C in its TG curve (Fig. S3). This loss can be attributed to the desorption of physisorbed water (m/z = 18 in Fig. S4). As the synthesis temperature was 550 °C, no significant thermal decomposition was observed in Figs. S3 and S4 below 550 °C, demonstrating good thermal stability of this material. Above 600 °C, ME-550-N primarily decomposes into fragments with m/z = 28 and 52 and almost completely gasified at 800 °C. Based on the elemental composition presented in Table 1, these species can be assigned to N_2 and C_2N_2, respectively. Moreover, high-sensitivity TPD detected additional gas emissions above 550 °C, including m/z = 2, 17, 18, 27, and 28. These can be attributed to H_2, NH_3/OH, H_2O, HCN, and N_2/CO. Consequently, a small fraction of O shown in Table 1 can be assigned to physisorbed water and oxygen-functional groups located at defect sites. The minor presence of O suggests a low level of defects in ME-550-N.

4.4. Spectroscopy (FTIR, DRS, PL) studies

4.4.1. FTIR

The FTIR spectra of the two sets of samples analyzed are shown in Fig. 4(A and B). The samples were measured in the spectral region 4000–500 cm^{-1}.

The band at 805 cm^{-1} belongs to the breathing mode of triazine units [78] and is present in each measured sample. In the spectral region between 1700 and 1100 cm^{-1} (areas A in Fig. 4), the sharp bands (at 1651 cm^{-1}, 1569 cm^{-1}, 1469 cm^{-1}, 1409 cm^{-1}, 1324 cm^{-1}, and 1239 cm^{-1}) are observed. These bands are assigned to the stretching vibrations of C=N and C-N bonds of heterocyclic rings [78,79].

The very broad bands appear between 3000 and 3700 cm^{-1} (areas B in Fig. 4). Bands at the spectral region are related to stretching vibration of N-H bonds [78–81]. The two bands (at approx. 3300 cm^{-1} and 3100 cm^{-1}) are clear visible in the spectra of samples treated by temperature 400 °C and 450 °C (in air atmosphere, as well as in nitrogen atmosphere). The bands are typical for asymmetrical (3300 cm^{-1}) and symmetrical (3100 cm^{-1}) stretching vibration of N-H bond of primary amines (R-NH_2). The similar "look" have the spectra of samples treated by temperature 500 °C (in both types of atmospheres), but both above mentioned spectral bands are almost overlapped. Only one band (at approx. 3080 cm^{-1}) is visible in the spectra of samples treated by temperature 550 °C (in both types of atmospheres). The band is due to stretching vibration of N-H bond of secondary amines (R_1-NH-R_2). With increasing heating temperature of melamine in air atmosphere, as well as in nitrogen atmosphere, N-H stretching vibrations are in FTIR spectra evident.

The elemental analysis indicates that the C/N ratio (mol.%) is approximately 0.67 and increases with increasing heating temperature of melamine in both atmospheres. However, this C/N ratio remains lower than the theoretical C/N ratio for g-C_3N_4 (0.75). It suggests that the amino groups are formed by incomplete condensation of the prepared g-C_3N_4. Residual hydrogen atoms are likely to bond to the edges of the graphene-like C-N sheets [82,83] in the form of C-NH_2 bonds (for temperature 400 °C–500 °C) and 2C-NH bonds (for temperature 550 °C).

4.4.2. Experimental (DRS)UV/Vis and calculated UV/Vis spectra analysis

The reflectance spectra of the prepared samples are shown in Fig. 5A–C. The indirect band gap energy values (Kubelka-Munk function, Tauc spectra) derived from the diffuse reflectance spectra (DRS) of ME samples subjected to thermal treatment at 400, 450, 500, and 550 °C in nitrogen (series N) and air (series A) atmospheres are shown in Fig. 5B, D and Table 2.

The band gap energy (E_g) values of melamine exhibited a decrease from 2.92 eV to 2.71 eV as the temperature of annealing increased in both nitrogen and air atmospheres. At the same temperature, there was no difference in the E_g of samples heat-treated in nitrogen or air. This finding is consistent with the red shift changes at the same temperature, which were almost identical in both nitrogen and air atmospheres

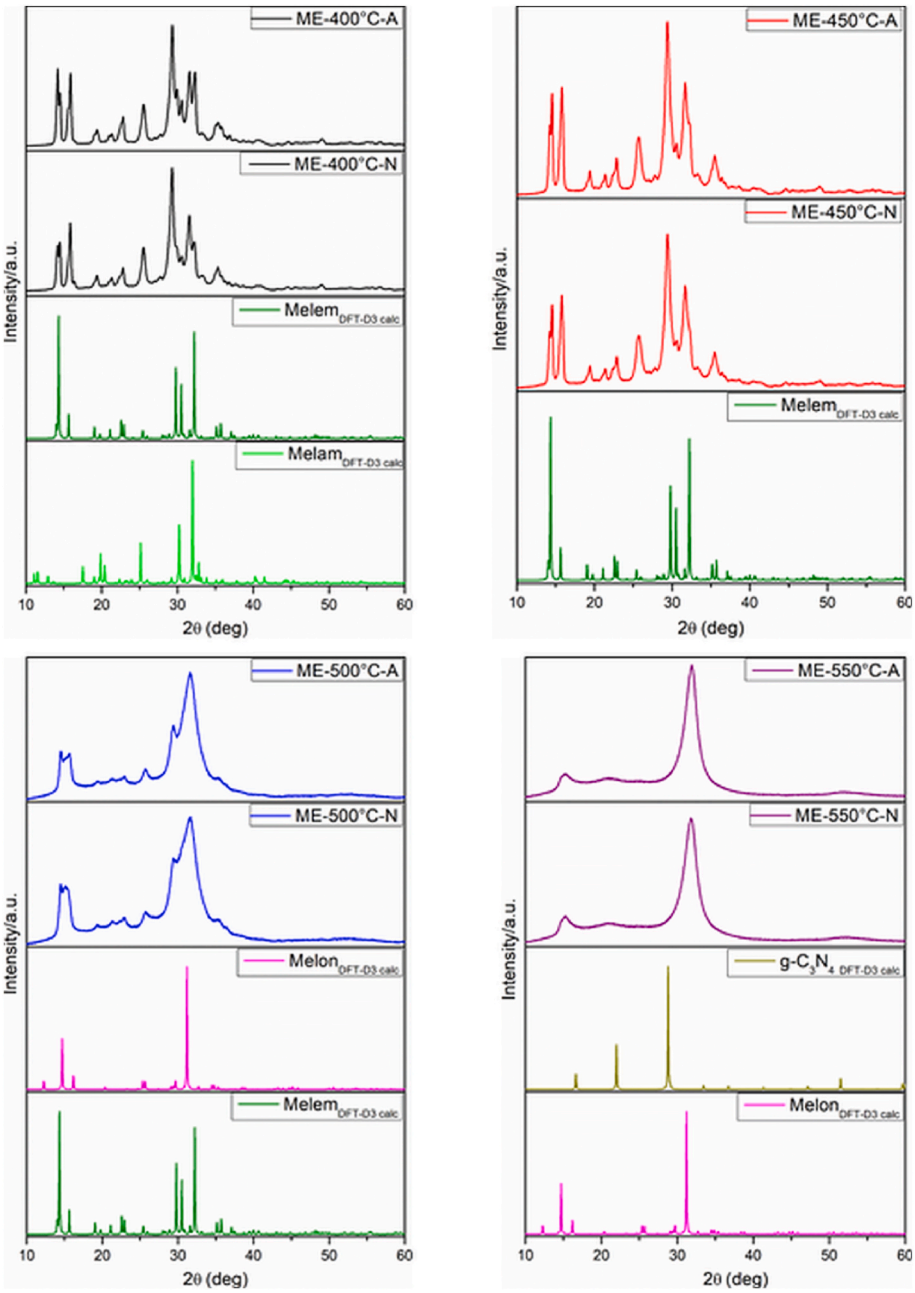

Fig. 3. Calculated (DFT-D3) and measured experimental XRD patterns of ME samples after thermal treatment at: 400, 450, 500, and 550 °C in nitrogen (N), and air (A) atmosphere.

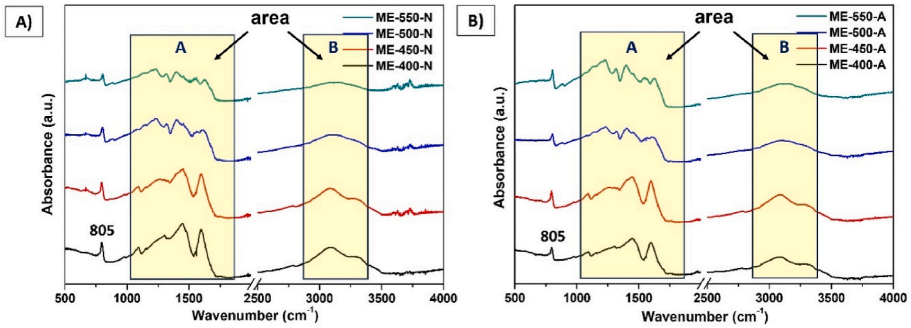

Fig. 4. IR spectra of ME samples after thermal treatment at 400, 450, 500, and 550 °C in (**A**) nitrogen (series **N**) and (**B**) air (series **A**) atmosphere.

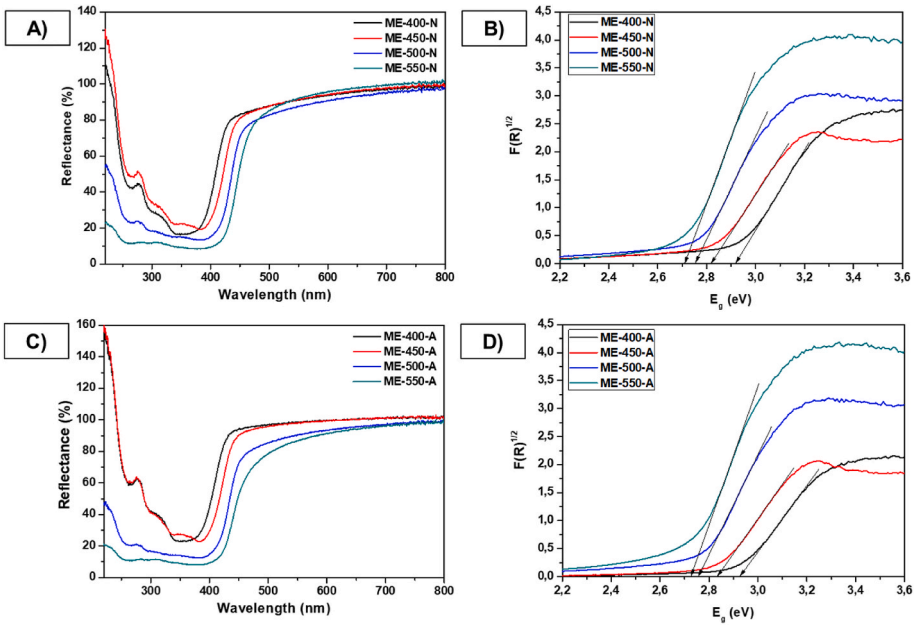

Fig. 5. Diffuse reflectance UV–Vis spectra (**A, C**) and Tauc spectra (**B, D**) at wavelengths from 220 to 800 nm of ME samples after thermal treatment at 400, 450, 500, and 550 °C in nitrogen (series **N**) and air (series **A**) atmosphere.

Table 2
Indirect band gap energy values (Kubelka-Munk function, Tauc spectra) from DRS spectra of ME samples after thermal treatment at 400, 450, 500, and 550 °C in nitrogen (series N) and air (series A) atmosphere.

Materials	E_g (eV)
ME-400-N	2.92
ME-450-N	2.82
ME-500-N	2.75
ME-550-N	2.71
ME-400-A	2.92
ME-450-A	2.83
ME-500-A	2.75
ME-550-A	2.72

(Fig. 5).

The DRS(UV–Vis) data for the samples synthesized at 400 °C (E_g = 2.92 eV) indicated the presence of melem as a dominant phase, with the remaining melam. This was confirmed by the theoretical and experimental studies. Upon increasing the heating temperature by 50 °C, a pristine melem structure was formed (E_g = 2.82 eV for sample ME-450-N and E_g = 2.83 eV for sample ME-450-A). At 500 °C, the melon structure predominates, with some remaining melem (E_g = 2.75 eV). The g-C_3N_4 structure was the predominant phase, with a residual melon content observed following the heating of melamine at 550 °C (E_g = 2.71 eV for sample ME-550-N, and E_g = 2.72 eV for sample ME-550-A). Vijayarangan et al. [84] have stated that at 350 °C the E_g is 2.89 eV (melam structure), at 400 °C the E_g value is 2.80 eV (melem structure), at 450 °C the E_g value is 2.72 eV (melon structure), while at the preparation temperature of 500 °C and 550 °C from melamine, E_g is then 2.64 eV (g-C_3N_4 structure), respectively.

The results obtained for this set of samples are highly comparable, with only minor discrepancies observed in the E_g values (see Table 2), which indicate excellent agreement with this study and with PL measurements (see Fig. 6, Table 3).

The experimental diffuse reflectance UV/Vis spectra of ME samples

Table 3
Maximum emission bands and evaluated E_g from PL spectra of ME samples after thermal treatment at 400, 450, 500, and 550 °C in nitrogen (series N) and air (series A) atmosphere.

Materials	Maximum emission bands (nm)/E_g (eV)
ME-400-N	422/(2.94)
ME-450-N	437/(2.84)
ME-500-N	459/(2.70)
ME-550-N	472/(2.63)
ME-400-A	422/(2.94)
ME-450-A	438/(2.83)
ME-500-A	456/(2.72)
ME-550-A	472/(2.63)

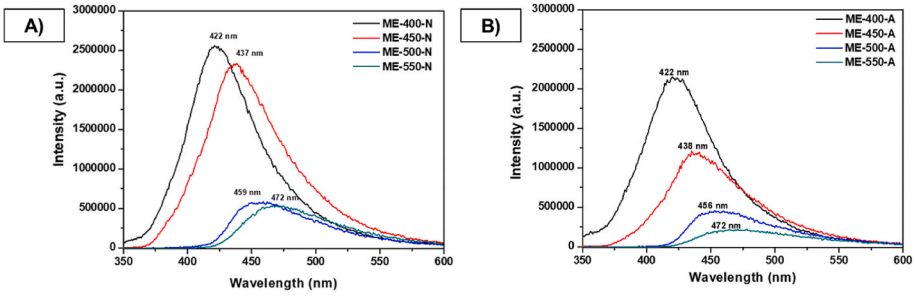

Fig. 6. PL spectra of ME samples after thermal treatment at 400, 450, 500, and 550 °C in nitrogen (**A**) and air (**B**) atmosphere.

after thermal treatment in the range of 400–550 °C in nitrogen (N) and air (A) atmosphere were also compared with calculated UV–Vis spectra of melam, melem, melon and g-C_3N_4 cluster models (Fig. S5). The computed models exhibited a red shift to lower energy levels, with the maximum absorbance observed at 235 nm for melam, 238 nm for melem, 296 nm for melon, and 304 nm for g-C_3N_4. The aforementioned red shift was also observed in the works of Lau et al. [77] and Liu et al. [74], which demonstrated a narrowing tendency of their band gaps.

4.4.3. Emission photoluminescence (PL) spectra

The emission photoluminescence (PL) spectra of the prepared samples are presented in Fig. 6, and Table 3 provides the positions of the maximum emission bands and E_g values evaluated from the PL spectra in the nitrogen and air atmosphere. In PL spectroscopy, the electrons in the valence band become excited after absorbing photons of suitable energy and reaching the conduction band edge. The emission of energy in the form of light occurs when the electrons reach a stable state at the valence band edge. The photoemission peak in PL spectra can be used to evaluate the band gap energy of a photocatalyst. A reduction in the photoemission peak indicates good charge carrier separation, which is required for an efficient photocatalyst.

Samples that have been annealed under a nitrogen atmosphere (Fig. 6A) demonstrate that as the annealing temperature increases, the emission bands are red-shifted to higher wavelengths from 422 nm to 472 nm (Table 3), and hence their intensity decreases. However, the intensities for samples ME-400-N and ME-450-N are considerably higher than those observed for samples prepared from melamine under an air atmosphere. PL measurements indicate that the degree of polycondensation of melamine in a nitrogen atmosphere is less pronounced, and that non-condensed amino groups can act as emission centres. It is noteworthy that the CN-N bond exhibits a relatively low PL emission peak, which may be attributed to its inconsistent structure, as evidenced by XRD [19,85].

Annealing in air (Fig. 6B), analogous to annealing in nitrogen, exhibits a shift of the emission bands' maxima with increasing temperature, from 422 nm to 472 nm (Table 3). However, the observed intensities were lower for the ME-400-A and ME-450-A samples, which could be attributed to a more effective separation of electrons and holes (h^+) [84]. The sample ME-450-A exhibits a phenomenon known as doublet emission, which can be attributed to the presence of structural elements within the system that originated from the C-N-H framework present in this melon phase [86]. A reduction in the magnitude of the transition energies associated with the temperature-induced polymerization of melamine has also been observed, as the HOMO (highest occupied molecular orbitals) and LUMO (lowest unoccupied molecular orbitals) energies have become increasingly similar [87].

The ME-500-A sample was found to exhibit a suppression of intensity and recombination of the charge carrier, as a result of the melon structure [88–91].

4.5. Morphology examination

The scanning electron microscopy (SEM) technique was employed to examine the morphology of the ME samples following thermal treatment at 400, 450, 500, and 550 °C in nitrogen (series **N**) and air (series **A**) atmospheres. All the powders exhibited a layered structure and a tendency to agglomerate (Fig. 7). Furthermore, the specific surface area ($\mathbf{S_{BET}}$) and physical parameters of mesopores/micropores from BET analysis of ME samples after thermal treatment at 400, 450, 500, and 550 °C in nitrogen (series **N**) and air (series **A**) atmosphere are provided in Supplementary Material (Table S3 and Fig. S6).

4.6. Degradation of AO7 under UV or VIS light

The photodegradation experiment comprises two distinct phases: (i) the dark phase and (ii) the irradiation phase. During the dark phase (first period without light illumination), an adsorption equilibrium was established for all samples, as indicated by the negligible variation in the relative concentration of AO7 during this period (see Fig. S7 in the Supplementary Material). The experiments were three times repeated, and to each of results the error bars (±5 %) are incorporated to reflect the variability in the measurements. Fig. 8 illustrates the changes in AO7 concentration with the duration of UV and VIS light irradiation (second period with light illumination) for the samples prepared in nitrogen and air atmospheres. The results of photodegradation activities (%) are included in Fig. S8. After 3 h of irradiation under UV or VIS light, the photocatalytic activities were between 70 and 99 % for samples heated in nitrogen and 50 and 99 % for samples heated in air, as shown in Fig. 8, Fig. S8 and Table 4. Furthermore, the photodegradation activity was found to be superior under UV light for both groups of samples. The activity of the ME samples (Fig. S8) was evaluated following thermal treatment at 400, 450, 500, and 550 °C in nitrogen and air atmospheres. The results are presented in Table 4 and Table S4, which compares the UV (360 nm) and VIS (420 nm) lamps. The sample heated at 500 °C (melon/melem) in an N_2 atmosphere revealed 75 % activity after 15 min under UV light and 22 % under VIS light, respectively. The ME-450-A (pristine melem) sample exhibited 76 % of the initial activity after 15 min of UV irradiation. The ME-500-A (melon/melem) sample demonstrated 10 % and 91 % of the initial photodegradation activity after 15 and 180 min of irradiation under visible light, respectively. It is

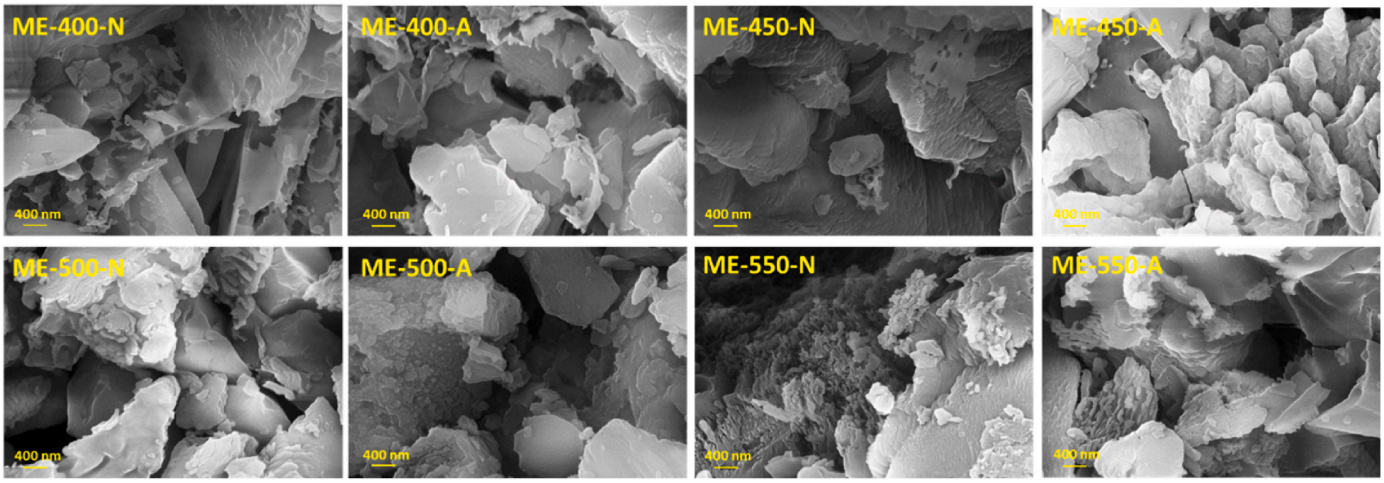

Fig. 7. SEM images of ME samples after thermal treatment at 400, 450, 500, and 550 °C in nitrogen (series N) and air (series A) atmosphere. MAG: 20.00 KX.

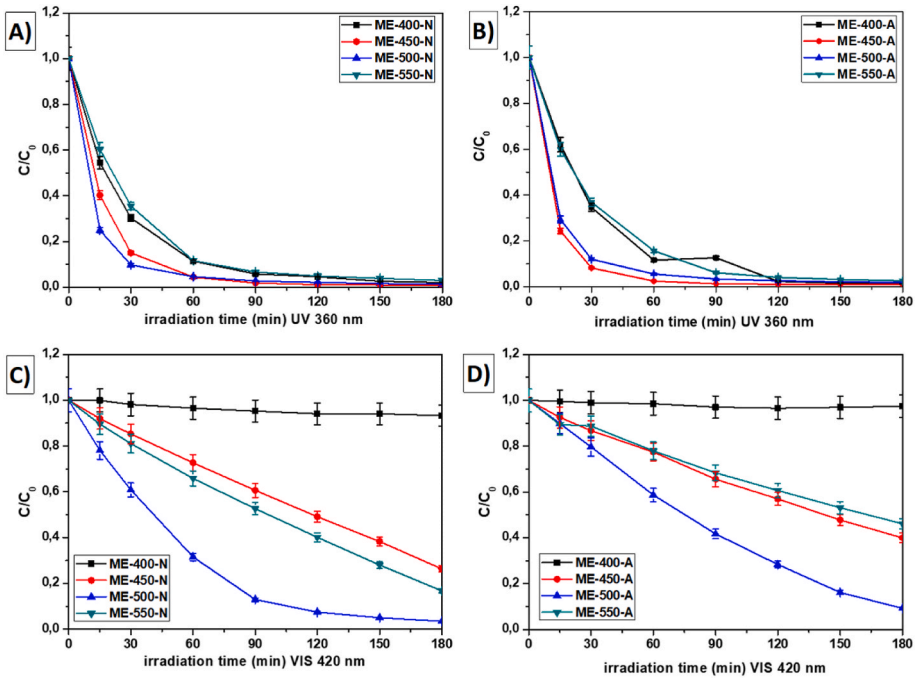

Fig. 8. Photocatalytic degradation processes C/C_0 of ME samples after thermal treatment at 400, 450, 500, and 550 °C in nitrogen (**A, C**) and air (**B, D**) atmosphere. Comparison of the UV lamp: 360 nm (**A, B**) vs. VIS lamp: 420 nm (**C, D**). Error bars representing a ±5 % variability.

Table 4
Activity and average kinetic constant (after 3 h) of ME samples after thermal treatment at 400, 450, 500, and 550 °C in nitrogen and air atmosphere. Comparison of the UV (360 nm) vs. VIS (420) nm lamps.

Materials	UV lamp		VIS lamp	
	Activity (%)	k_{cal} 10^{-3} (min^{-1})	Activity (%)	k_{cal} 10^{-3} (min^{-1})
ME-400-N	98	31.0	7	0.4
ME-450-N	99	45.0	74	5.9
ME-500-N	99	49.0	97	19.3
ME-550-N	97	29.0	83	7.3
ME-400-A	99	30.0	3	0.3
ME-450-A	99	55.0	60	4.8
ME-500-A	98	45.0	91	9.9
ME-550-A	97	28.0	54	4.6

noteworthy that this is the first instance of a straightforward approach that is scalable, cost-effective, and environmentally benign in achieving metal-free photocatalysts based on graphitic carbon nitride compounds derived from melamine. Furthermore, the process of thermal treatment in nitrogen or air at temperatures ranging from 400 to 550 °C, involving a mere 30-min holding period at the selected temperature, is also worthy of mention. The proposed novel approach to the development of g-C_3N_4-based materials demonstrates that organic composites created at lower temperatures display the highest photocatalytic properties, allowing for the reduction of time, energy, and financial resources typically required for the manufacturing of high-quality photocatalysts.

Fig. 8 also illustrates the differences in the degradation rates of the nitrogen and air series under UV and VIS light, with the data supported by the calculated kinetic constants (Table 4). The calculated kinetic constants (k_{cal}) were determined for all materials using the pseudo-first-order reaction equation $\ln(C/C_0) = -k_{cal}t$, where C_0 is the initial concentration of AO7, C is the concentration of AO7 at the time t of the measurement, and k is the kinetic constant [26,92,93]. The logarithmic plots of the degradation studies with the kinetic rate constants as a function of UV or VIS irradiation time are included in Figs. S9 and S10. The average kinetic constants obtained for the samples heat-treated in a nitrogen atmosphere were found to be in the ranges of 29–49 × 10^{-3} min^{-1} (under UV lamp) and 0.4–19.3 × 10^{-3} min^{-1} (under VIS lamp), respectively. The determined average kinetic constants for the series of materials synthesized in an air atmosphere were in the ranges of 28–55 × 10^{-3} min^{-1} and 0.3–9.9 × 10^{-3} min^{-1}, respectively, under UV and VIS light. It can be observed that with increasing temperature from 400 to 500 °C, the average kinetic constant parameters increase as well for both series of samples, and this phenomenon was registered under both wavelengths of light. When the annealing temperature of melamine reached the value of 550 °C under a nitrogen or air atmosphere and pristine g-C_3N_4 material was obtained, the values of the average kinetic constant decreased by approximately twofold.

In order to facilitate a comparison of the results obtained from samples heat-treated at 500 and 550 °C in an air, two samples were synthesized and labelled R-520-4 h and R-550-2 h. The synthesis conditions were documented, as well as the results of physicochemical examinations, including XRD, DRS (UV–VIS), and photodegradation experiments towards AO7 dye under UV and VIS lights. Furthermore, the theoretical calculations performed using the Density Functional Theory (DFT) method provided additional insight into the experimental XRD data.

The Supplementary Material (Fig. S11 to Fig. S18, Table S5) contains and discusses all this information. Furthermore, a literature review of g-C_3N_4 (g-CN) - based composites used for photodegradation of selected dyes is included in Table S6. Hence, it can be concluded that the best photocatalytic properties were estimated for g-C_3N_4-based materials that represented organic/organic composites like: melem/melon, or melon/g-C_3N_4.

4.7. Scavengers measurements

As previously stated, scavenger experiments represent an invaluable tool for elucidating the participation of specific forms of radicals or other forms/species, such as holes, in the photodegradation process. Fig. 9

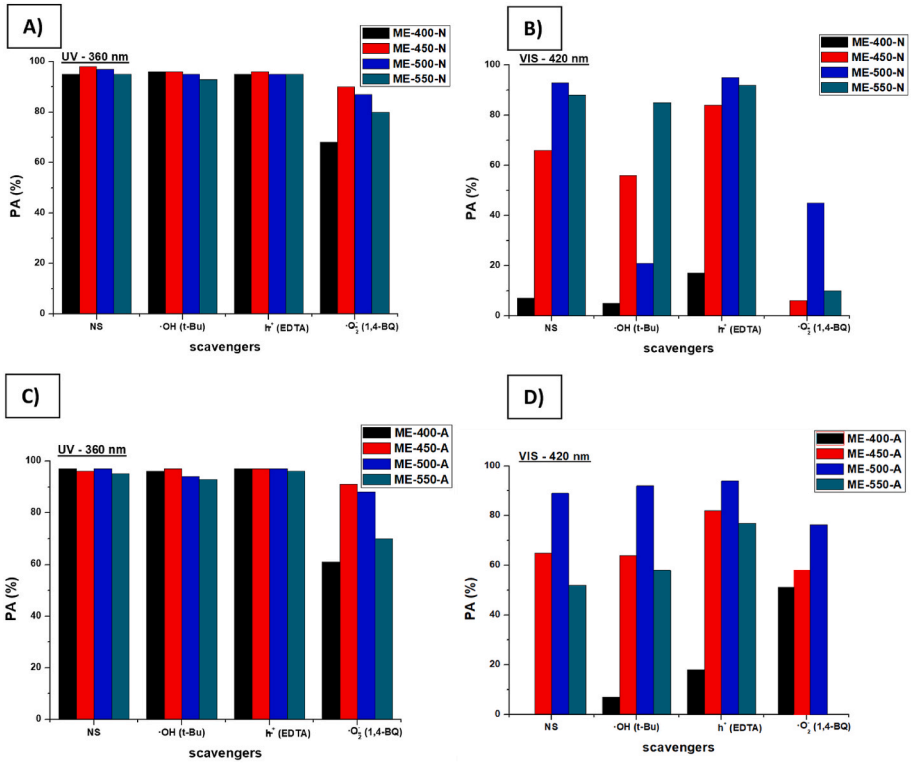

Fig. 9. Scavengers experiments of ME samples after thermal treatment at 400, 450, 500, and 550 °C in nitrogen (series **N**) (A, B) and air (series **A**) atmosphere (C, D).

depicts scavenger experiments conducted on ME samples following thermal treatment at 400, 450, 500, and 550 °C in nitrogen (series N) (Fig. 9A and B) and air (series A) atmospheres (Fig. 9C and D).

A comparison of ME samples of the N series under UV irradiation reveals that only the ME-400-N* sample exhibits the participation of superoxide radicals ($^{\bullet}O_2^-$) in AO7 photodegradation. A comparable situation is evident for the sample ME-550-N*, where the $^{\bullet}O_2^-$ plays a dominant role in AO7 photodegradation in the absence of the scavenger. The impact of these superoxide radicals is somewhat lower for this sample. It can be seen that the masking of superoxide radicals results in a reduction in the photodegradation activity of AO7 for the aforementioned samples. A notable impact of superoxide radicals (very high photoactivity, but lower than for no scavengers (NS) was observed for samples ME-450-N* and ME-500-N*. Other species (h^+ and $^{\bullet}OH$) did not result in a decrease in photoactivity for AO7. On the contrary, they are higher than for NS (no scavenger), therefore do not participate in photodegradation. Furthermore, it can be stated that these reactions can occur as oxidation/reduction processes (1)–(7) [93–99]:

Photoexcitation process:

$$g\text{-}C_3N_4 + hv \rightarrow e^- + h^+ \quad (1)$$

Oxygen ionosorption process:

$$O_2 + e^- \rightarrow {}^{\bullet}O_2^- \quad (2)$$

Ionization of water:

$$H_2O \rightarrow OH^- + H^+ \quad (3)$$

Protonation of superoxide from water:

$${}^{\bullet}O_2^- + H^+ \rightarrow HO_2^{\bullet} \quad (4)$$

Co-scavenging of e^-:

$$HO_2^{\bullet} + e^- \rightarrow HO_2^- \quad (5)$$

Formation of H_2O_2:

$$HO_2^- + H^+ \rightarrow H_2O_2 \quad (6)$$

$$\text{pollutant} + e^- \rightarrow \text{reduction products} \quad (7)$$

The aforementioned results, which relate to the preparation of samples under a nitrogen atmosphere and the perspective of scavengers, have not yet been published.

Another scenario is that of ME samples subjected to thermal treatment at temperatures of 400, 450, 500, and 550 °C in a nitrogen

Table 5
Scavengers experiments after thermal treatment at 400, 450, 500, and 550 °C in a nitrogen atmosphere. Comparison of the UV (360 nm) vs. VIS (420) nm lamps.

materials	holes (h^+) ethylenediamine-tetraacetic acid (EDTA)	superoxide radicals ($^{\bullet}O_2^-$) 1,4-benzoquinone (1,4-BQ)	hydroxyl radicals ($^{\bullet}OH$) t-butanol (t-Bu)
ME-400-N[a]	–	++	–
ME-450-N[a]	–	~	–
ME-500-N[a]	–	~	–
ME-550-N[a]	–	+	–
ME-400-N[b]	–	++	–
ME-450-N[b]	–	+++	+
ME-500-N[b]	–	++	+++
ME-550-N[b]	–	+++	~

[a] UV irradiation.
[b] VIS irradiation, - without influence, ~ very weak influence, + weak influence, ++ strong influence, +++ very strong influence.

atmosphere (series N) and subsequently irradiated with visible light (VIS), as illustrated in Fig. 9B. As can be seen from Table 5, in addition to the action of superoxide radicals and hydroxyl radicals (•OH), the photodegradation of AO7 in VIS is also significantly influenced by the presence of scavenger t-butanol (t-Bu). This is evident for the sample ME-500-N** prepared in a nitrogen atmosphere.

It was observed that the highest decrease in photoactivity for AO7 occurred in the sample ME-550-N**, where a significant effect on the photoactivity of peroxide radicals and very little hydroxide radicals was evident. Conversely, the ME-500-N** sample demonstrated a significant influence of AO7 on the photoactivity of both hydroxyl and superoxide radicals.

In addition to the aforementioned reactions (1)–(7), further reactions will also occur (8 and 9) [93–99]:

Formation of •OH:

$$H_2O_2 + e^- \rightarrow {}^{\bullet}OH + OH^- \quad (8)$$

$$\text{pollutant} + {}^{\bullet}OH \rightarrow \text{degradation products} \quad (9)$$

It can be observed that, once again, the holes do not participate in the photodegradation of AO7 when the samples are irradiated with VIS light. This is the case for the series of samples (ME-400-N to 550-N**).

The situation is markedly different in the case of the ME-400-A to ME-550-A series, particularly during irradiation under visible light (VIS), as illustrated in Table 6 and Fig. 9D, in comparison to the ME-400-N to ME-550-N series, where it is evident that the ME-550-A** sample exerts the greatest influence on the photoactivity in VIS during photodegradation at AO7. Furthermore, it is evident that the scavenger ethylenediamine-tetraacetic acid (EDTA) and hydroxyl radicals (•OH) are ineffective when used in conjunction with holes (h^+), as observed when employing the scavenger t-butanol (t-Bu).

A strong influence of superoxide radicals was also detected in samples ME-400-A* and ME-550-A* (UV irradiation), as illustrated in Fig. 9C and Table 6. In contrast, photoactivity was found to be very low in these samples at AO7 [59,100].

It can be reasonably assumed that the oxygen vacancies and the individual types of materials present in the prepared A-series samples (mixtures based on melem, melon, melam or g-C_3N_4) result in the formation of n-n^+ heterojunctions. This is thought to improve charge separation and increase charge transfer at the interface between the liquid and the solid, due to the presence of the prepared nanoparticles in the samples. This process is believed to significantly enhance the photoactivity of the samples in comparison to AO7 [101,102]. A very slight influence of superoxide radicals was again observed and found for samples ME-450-A* and ME-500-A* (UV irradiation). Furthermore, as previously stated, no influence of holes and hydroxyl radicals on the photodegradation of AO7 was observed in the case of using EDTA and t-Bu scavengers, see Table 6 and Fig. 9C, same for ME-400-A to 550-A** series, see Fig. 9D and Table 6 [26,59,60,100]. The following reactions will also occur (1) to (7), as described above, in both series (ME-400-A to ME-550-A* and ME-400-A to ME-550-A**).

Table 6
Scavengers experiments after thermal treatment at 400, 450, 500, and 550 °C in air atmosphere. Comparison of the UV (360 nm) vs. VIS (420) nm lamps.

materials	holes (h^+) ethylenediamine-tetraacetic acid (EDTA)	superoxide radicals ($^{\bullet}O_2^-$) 1,4-benzoquinone (1,4-BQ)	hydroxyl radicals (•OH) t-butanol (t-Bu)
ME-400-A[a]	–	++	–
ME-450-A[a]	–	~	–
ME-500-A[a]	–	~	–
ME-550-A[a]	–	++	–
ME-400-A[b]	–	–	–
ME-450-A[b]	–	~	–
ME-500-A[b]	–	+	–
ME-550-A[b]	–	+++	–

[a] UV irradiation.
[b] VIS irradiation, - without influence, ~ very weak influence, + weak influence, ++ strong influence, +++ very strong influence.

5. Conclusions

A facile, scalable, and low-cost method was proposed for the synthesis of metal-free photocatalysts based on graphitic carbon nitride compounds derived from melamine. The method involved a 30-min thermal treatment in either nitrogen or air at temperatures ranging from 400 to 550 °C. The effect of temperature and atmosphere on the degradation of the model acid orange 7 dye under UV or visible light irradiation was evaluated.

The X-ray diffraction (XRD) results aligned with the elemental analysis. In this study, density functional theory (DFT) with the D3 dispersion correction (DFT-D3) method was employed to support the experimental findings. The calculated DFT-D3 results demonstrated a strong correlation with the XRD experimental data, indicating that the reflections of the studied crystal structures gradually disappeared from the XRD pattern as the temperature increased. This observation was further confirmed by the red shift observed in the ultraviolet–visible (UV–VIS) spectra, which indicated a shift to lower energy levels. The results of the diffuse reflectance spectroscopy DRS (UV–VIS) analysis were consistent with those of photoluminescence (PL) spectroscopy.

Following a prolonged irradiation period (3 h) under UV or VIS light, the photocatalytic activities were observed to be 70 and 99 % for samples heated in nitrogen, and 50 and 99 % for samples heated in air, respectively. Both cases demonstrated superior activity under UV light. The sample heated at 500 °C in an N_2 atmosphere revealed 75 % activity after 15 min under UV light and 22 % under VIS light, respectively. Sample ME-450-A had 76 % activity after 15 min under UV irradiation. The sample ME-500-A showed 10 % and 91 % of photocatalytic activity after 15 and 180 min of irradiation under VIS light, respectively.

A principal outcome of this research is the demonstration that enhanced photocatalytic efficiency can be achieved through the use of organic composites synthesized at relatively lower temperatures, eliminating the need for conventional modifications such as the incorporation of transition metal oxides (TMO). This approach reduces both energy consumption and manufacturing costs while maintaining high photocatalytic efficiencies, offering a more sustainable pathway for the development of photocatalysts.

Moreover, the first comprehensive comparison of g-C_3N_4-based materials synthesized in nitrogen and air atmospheres revealed significant differences in photocatalytic efficiencies, addressing a critical gap in the literature. The application of advanced analytical techniques, including thermogravimetry-differential scanning calorimetry coupled with mass spectrometry (TG-DSC-MS) and temperature-programmed desorption (TPD), provided valuable insights into the thermal stability and structural transformations of the synthesized materials, enhancing our understanding of their behavior under varying conditions.

In conclusion, this research presents a pioneering approach to the synthesis of g-C_3N_4-based photocatalysts, demonstrating that high photocatalytic efficiency can be achieved through a simple, time-efficient process. The findings offer significant implications for the future design of cost-effective, environmentally friendly photocatalysts for practical applications in environmental remediation and beyond.

CRediT authorship contribution statement

Monika Michalska: Writing – review & editing, Writing – original draft, Visualization, Validation, Supervision, Resources, Project administration, Methodology, Investigation, Funding acquisition, Formal analysis, Data curation, Conceptualization. **Jiri Pavlovsky:** Writing – review & editing, Writing – original draft, Visualization, Methodology, Investigation, Formal analysis. **Eva Scholtzova:** Writing – review & editing, Writing – original draft, Visualization, Resources, Methodology, Funding acquisition, Formal analysis. **Peter Skorna:** Writing – original draft, Visualization, Resources, Formal analysis. **Vlastimil Matejka:** Investigation. **Kamil Bochenek:** Investigation. **Amrita Jain:** Writing – review & editing, Investigation, Funding acquisition. **Koki Chida:** Investigation. **Takeharu Yoshii:** Investigation. **Hirotomo Nishihara:** Writing – original draft, Funding acquisition, Formal analysis.

Declaration of competing interest

The authors declare that they have no known competing financial interests or personal relationships that could have appeared to influence the work reported in this paper.

Acknowledgments

The authors would like to thank Dr. K. Foniok (VSB-TUO) for BET measurements.

This work was financially supported by the Ministry of Education, Youth and Sports, Czech Republic (contract no. 8F21007), Slovak Academy of Sciences, Slovakia (V4-Japan/JRP/2021/96/AtomDeC), National Center for Research and Development, Poland (V4-Japan/2/17/AtomDeC/2022), and the Japan Science and Technology Agency JST SICORP Grant No. JPMJSC2112 through the research project cooperation between the AtomDeC Consortium by funding received from the Visegrad group(V4)-Japan 2021 2nd Joint Call on "Advanced Materials". The authors also thank the Large Research Infrastructure ENREGAT, supported by the Ministry of Education, Youth and Sports, Czech Republic (Project No. LM2023056).

Appendix A. Supplementary data

Supplementary data to this article can be found online at https://doi.org/10.1016/j.rineng.2024.103109.

Abbreviations:

AO7	acid orange 7
CDA	cyanamide
DCDA	dicyandiamide
GUA	guanidine hydrochloride
HR	heating rate
ME	melamine
PA	Photodegradation activity
RhB	rhodamine B
UR	urea

Data availability

Data will be made available on request from the corresponding author (Dr. Monika Michalska, monika.kinga.michalska@gmail.com).

References

[1] D. Vaya, B. Kaushik, P.K. Surolia, Recent advances in graphitic carbon nitride semiconductor: structure, synthesis and applications, Mater. Sci. Semicond. Process. 137 (2022) 106181.
[2] M. Inagaki, T. Tsumura, T. Kinumoto, M. Toyoda, Graphitic carbon nitrides ($g\text{-}C_3N_4$) with comparative discussion to carbon materials, Carbon 141 (2019) 580–607.
[3] E.O. Oseghe, S.O. Akpotu, E.T. Mombeshora, A.O. Oladipo, L.M. Ombaka, B. C. Maria, A.O. Idris, G. Mamba, L. Ndlwana, O.S. Ayanda, A.E. Ofomaja, V. O. Nyamori, U. Feleni, T.T.I. Nkambule, T.A.M. Msagati, B.B. Mamba, D. W. Bahnemann, Multi-dimensional applications of graphitic carbon nitride nanomaterials – a review, J. Mol. Liq. 344 (2021) 117820.
[4] G. Mamba, A.K. Mishra, Graphitic carbon nitride ($g\text{-}C_3N_4$) nanocomposites: a new and exciting generation of visible light driven photocatalysts for environmental pollution remediation, Appl. Catal., B 198 (2016) 347–377.
[5] W.-J. Ong, L.-L. Tan, Y.H. Ng, S.-T. Yong, S.-P. Chai, Graphitic carbon nitride ($g\text{-}C_3N_4$)-based photocatalysts for artificial photosynthesis and environmental remediation: are we a step closer to achieving sustainability? Chem. Rev. 116 (2016) 7159–7329.
[6] M.P. Rayaroth, G. Lee, Y.-S. Chang, Recent developments in graphitic carbon nitride ($g\text{-}C_3N_4$) applications in micromotors, Results Eng 22 (2024) 102244.
[7] T. Yoshii, K. Tamaki, Y. Kuwahara, K. Mori, H. Yamashita, Self-assembled core–shell nanocomposite catalysts consisting of single-site Co-coordinated $g\text{-}C_3N_4$ and Au nanorods for plasmon-enhanced CO_2 reduction, J. CO_2 Util. 52 (2021) 101691.
[8] A. Al-Ahmed, Photocatalytic properties of graphitic carbon nitrides ($g\text{-}C_3N_4$) for sustainable green hydrogen production: recent advancement, Fuel 316 (2022) 123381.
[9] Z. Zhang, Y. Zhang, L. Lu, Y. Si, S. Zhang, Y. Chen, K. Dai, P. Duan, L. Duan, J. Liu, Graphitic carbon nitride nanosheet for photocatalytic hydrogen production: the impact of morphology and element composition, Appl. Surf. Sci. 391 (2017) 369–375.
[10] S. Yang, Y. Gong, J. Zhang, L. Zhan, L. Ma, Z. Fang, R. Vajtai, X. Wang, P. M. Ajayan, Exfoliated graphitic carbon nitride nanosheets as efficient catalysts for hydrogen evolution under visible light, Adv. Mater. 25 (2013) 2452–2456.
[11] S.M. Abu-Sari, W.M.A.W. Daud, M.F.A. Patah, B.C. Ang, Sulfur self-doped $g\text{-}C_3N_4$ nanofiber modified by NiO co-catalyst: an efficient, collectible, durable, and low-cost photocatalyst for visible-light-driven hydrogen evolution from water, Results Eng 17 (2023) 100952.
[12] G.-Q. Zhao, J. Zou, J. Hu, X. Long, F.-P. Jiao, A critical review on graphitic carbon nitride ($g\text{-}C_3N_4$)-based composites for environmental remediation, Sep. Purif. Technol. 279 (2021) 119769.
[13] Y. Zhang, J. Yuan, Y. Ding, B. Liu, L. Zhao, S. Zhang, Research progress on $g\text{–}C_3N_4$–based photocatalysts for organic pollutants degradation in wastewater: from exciton and carrier perspectives, Ceram. Int. 47 (2021) 31005–31030.
[14] A. Wang, C. Wang, L. Fu, W. Wong-Ng, Y. Lan, Recent advances of graphitic carbon nitride-based structures and applications in catalyst, sensing, imaging, and LEDs, Nano-Micro Lett. 9 (2017) 1–21.
[15] I. Ibrahim, G.V. Belessiotis, M. Antoniadou, A. Kaltzoglou, E. Sakellis, F. Katsaros, L. Sygellou, M.K. Arfanis, T.M. Salama, P. Falaras, Silver decorated $TiO_2/g\text{-}C_3N_4$ bifunctional nanocomposites for photocatalytic elimination of water pollutants under UV and artificial solar light, Results Eng 14 (2022) 100470.
[16] K. Cheng, T. Zhang, R. Xiong, H. Li, G. Wu, W. Xing, Synergetic contribution of carbon and oxygen co-doped carbon nitride nanosheets as metal-free photocatalysts for wastewater purification, Results Eng 17 (2023) 100956.
[17] M. Hosseini, M. Ghanbari, E.A. Dawi, M.H.S. Alubiady, A.M. Al-Ani, A.F. Alkaim, M. Salavati-Niasari, $CaSnO_3/g\text{-}C_3N_4$ S-scheme heterojunction photocatalyst for the elimination of erythrosine and eriochrome black T from water under visible light, Results Eng 21 (2024) 101903.
[18] I. Mohammadi, F. Zeraatpisheh, E. Ashiri, K. Abdi, Solvothermal synthesis of $g\text{-}C_3N_4$ and ZnO nanoparticles on TiO_2 nanotube as photoanode in DSSC, Int. J. Hydrogen Energy 45 (2020) 18831–18839.
[19] F. Dong, Z. Zhao, T. Xiong, Z. Ni, W. Zhang, Y. Sun, W.-K. Ho, In situ construction of $g\text{-}C_3N_4/g\text{-}C_3N_4$ metal-free heterojunction for enhanced visible-light photocatalysis, ACS Appl. Mater. Interfaces 5 (2013) 11392–11401.
[20] G. Zhang, J. Zhang, M. Zhang, X. Wang, Polycondensation of thiourea into carbon nitride semiconductors as visible light photocatalysts, J. Mater. Chem. 22 (2012) 8083–8091.
[21] C. Liu, X. Dong, Y. Hao, X. Wang, H. Ma, X. Zhang, A novel supramolecular preorganization route for improving $g\text{-}C_3N_4/g\text{-}C_3N_4$ metal-free homojunction photocatalysis, New J. Chem. 41 (2017) 11872–11880.
[22] I. Papailias, T. Giannakopoulou, N. Todorova, D. Demotikali, T. Vaimakis, C. Trapalis, Effect of processing temperature on structure and photocatalytic properties of $g\text{-}C_3N_4$, Appl. Surf. Sci. 358 (2015) 278–286.
[23] T.S. Miller, A.B. Jorge, T.M. Suter, A. Sella, F. Cora, P.F. McMillan, Carbon nitrides: synthesis and characterization of a new class of functional materials, Phys. Chem. Chem. Phys. 19 (2017) 15613–15638.
[24] G. Dong, Y. Zhang, Q. Pan, J. Qiu, A fantastic graphitic carbon nitride ($g\text{-}C_3N_4$) material: electronic structure, photocatalytic and photoelectronic properties, J. Photochem. Photobiol., A 20 (2014) 33–50.
[25] B. Jürgens, E. Irran, J. Senker, P. Kroll, H. Müller, W. Schnick, Melem (2,5,8-triamino-tri-s-triazine), an important intermediate during condensation of melamine rings to graphitic carbon nitride: synthesis, structure determination by X-ray powder diffractometry, solid-state NMR, and theoretical studies, Am. Chem. Soc. 125 (2003) 10288–10300.
[26] M. Michalska, V. Matejka, J. Pavlovsky, P. Praus, M. Ritz, J. Serencisova, L. Gembalova, M. Kormunda, K. Foniok, M. Reli, G. Simha Martynkova, Effect of Ag modification on TiO_2 and melem/$g\text{-}C_3N_4$ composite on photocatalytic performances, Sci. Rep. 13 (2023) 5270.

[27] S. Yang, W. Zhou, C. Ge, X. Liu, X. Fang, Z. Li, Mesoporous polymeric semiconductor materials of graphitic-C_3N_4: general and efficient synthesis and their integration with synergistic AgBr NPs for enhanced photocatalytic performances, RSC Adv. 3 (2013) 5631–5638.

[28] Y. Gao, W. Zhao, D. Zhang, Preparation of prismatic g-C_3N_4 by CTAB hydrothermal method and its degradation performance under visible light, Diam. Relat. Mater. 121 (2022) 108787.

[29] X. Wu, F. Chen, X. Wang, H. Yu, In situ one-step hydrothermal synthesis of oxygen-containing groups-modified g-C_3N_4 for the improved photocatalytic H_2-evolution performance, Appl. Surf. Sci. 427 (2018) 645–653.

[30] C. Hu, Y.-C. Chu, M.-S. Wang, X.-H. Wu, Rapid synthesis of g-C_3N_4 spheres using microwave-assisted solvothermal method for enhanced photocatalytic activity, J. Photochem. Photobiol., A 348 (2017) 8–17.

[31] X. Bai, J. Li, C. Cao, S. Hussain, Solvothermal synthesis of the special shape (deformable) hollow g-C_3N_4 nanospheres, Mater. Lett. 65 (2011) 1101–1104.

[32] Y. Ciu, Y. Tang, X. Wang, Template-free synthesis of graphitic carbon nitride hollow spheres for photocatalytic degradation of organic pollutants, Mater. Lett. 161 (2015) 197–200.

[33] H.R. Allcock, F.W. Lampe, Contemporary Polymer Chemistry, Prentice Hall, New Jersey, 1990.

[34] W.C. Kuryla, A.J. Papa, Flame Retardancy of Polymeric Materials, vols. 1–5, Dekker, New York, 1973–1979.

[35] L.F. Lindoy, I.M. Atkinson, Self-assembly in supramolecular systems. Monographs in Supramolecular Chemistry, Cambridge, New York, 2000, 7.

[36] J.W. Steed, J.L. Atwood, Supramolecular Chemistry, John Wiley & Sons, Ltd., Chichester, New York, Weinheim, Brisbane, Singapore, Toronto, 2000.

[37] N. Kimizuka, T. Kawasaki, K. Hirata, T. Kunitake, Tube-like nanostructures composed of networks of complementary hydrogen bonds, J. Am. Chem. Soc. 117 (1995) 6360–6361.

[38] I. Alves, G. Demazeau, B. Tanguy, F. Weill, On a new model of the graphitic form of C_3N_4, Solid State Commun. 109 (1999) 697–701.

[39] Z. Zhang, K. Leinenweber, M. Bauer, L.A.J. Garvie, P.F. McMillan, G.H. Wolf, High-pressure bulk synthesis of crystalline $C_6N_9H_3{\cdot}HCl$: a novel C_3N_4 graphitic derivative, J. Am. Chem. Soc. 123 (2001) 7788–7796.

[40] G.H. Wolf, M. Bauer, K. Leinenweber, L.A.J. Garvie, Z. Zhang, NATO Sci. Ser., II: mathematics, physics and Chemistry 48, Frontiers of High-Pressure Research II: Application of High Pressure to Low-Dimensional NoVel Electronic Materials) 29 (2001).

[41] M. Kawaguchi, K. Nozaki, Synthesis, structure, and characteristics of the new host material $[(C_3N_3)_2(NH)_3]_n$, Chem. Mater. 7 (1995) 257–264.

[42] V.N. Khabashesku, J.L. Zimmermann, J.L. Margrave, Powder synthesis and characterization of amorphous carbon nitride, Chem. Mater. 12 (2000) 3264–3270.

[43] E.G. Gillan, Synthesis of nitrogen-rich carbon nitride networks from an energetic molecular azide precursor, Chem. Mater. 12 (2000) 3906–3912.

[44] A.Y. Liu, M.L. Cohen, Prediction of new low compressibility solids, Science 245 (1989) 841–842.

[45] D.M. Teter, R.J. Hemley, Low-Compressibility carbon nitrides, Science 271 (1996) 53–55.

[46] M. Mattesini, S.F. Matar, J. Etourneau, Stability and electronic property investigations of the graphitic C_3N_4 system showing an orthorhombic unit cell, J. Mater. Chem. 10 (2000) 709–713.

[47] W. Yu, T. Yoshii, A. Aziz, R. Tang, Z.-Z. Pan, K. Inoue, M. Kotani, H. Tanaka, E. Scholtzová, D. Tunega, Y. Nishina, K. Nishioka, S. Nakanishi, Y. Zhou, O. Terasaki, H. Nishihara, Edge-Site-free and topological-defect-rich carbon cathode for high-performance lithium-oxygen batteries, Adv. Sci. 10 (2023) 2300268.

[48] X. Yuan, K. Luo, N. Liu, X. Ji, C. Liu, J. He, G. Tian, Y. Zhao, D. Yu, Cluster-model DFT simulations of the infrared spectra of triazine-based molecular crystals, Phys. Chem. Chem. Phys. 20 (2018) 20779–20784.

[49] M.J. Bojdys, J.-O. Muller, M. Antonietti, A. Thomas, Ionothermal synthesis of crystalline, condensed, graphitic carbon nitride, Chem. Eur J. 14 (2008) 8177–8182.

[50] B.V. Lotsch, M. Doblinger, J. Sehnert, L. Seyfarth, J. Senker, O. Oeckler, W. Schnick, Unmasking melon by a complementary approach employing electron diffraction, solid-state NMR spectroscopy, and theoretical calculations—structural characterization of a carbon nitride polymer, Chem. Eur J. 13 (2007) 4969–4980.

[51] Y. Tao, Q. Ni, M. Wei, D. Xia, X. Li, A. Xu, Metal-free activation of peroxymonosulfate by g-C_3N_4 under visible light irradiation for the degradation of organic dyes, RSC Adv. 5 (2015) 44128–44136.

[52] S. Ganesan, T. Kokulnathan, S. Sumathi, A. Palaniappan, Efficient photocatalytic degradation of textile dye pollutants using thermally exfoliated graphitic carbon nitride (TE–g–C_3N_4), Sci. Rep. 14 (2024) 2284.

[53] P. Praus, A. Smýkalová, K. Foniok, V. Matějka, M. Kormunda, B. Smetana, D. Cvejn, The presence and effect of oxygen in graphitic carbon nitride synthetized in air and nitrogen atmosphere, Appl. Surf. Sci. 529 (2020) 147086.

[54] R.A. Senthil, J. Theerthagiri, A. Selvi, J. Madhavan, Synthesis and characterization of low-cost g-C_3N_4/TiO_2 composite with enhanced photocatalytic performance under visible-light irradiation, Opt. Mater. 64 (2017) 533–539.

[55] L. Ming, H. Yue, L. Xu, F. Chen, Hydrothermal synthesis of oxidized g-C_3N_4 and its regulation of photocatalytic activity, J. Mater. Chem. A 2 (2014) 19145–19149.

[56] T. Xia, T. Yoshii, K. Nomura, K. Wakabayashi, Z.-Z. Pan, T. Ishii, H. Tanaka, T. Mashio, J. Miyawaki, T. Otomo, K. Ikeda, Y. Sato, M. Terauchi, T. Kyotani, H. Nishihara, Chemistry of zipping reactions in mesoporous carbon consisting of minimally stacked graphene layers, Chem. Sci. 14 (2023) 8448–8457.

[57] K. Wakabayashi, T. Yoshii, H. Nishihara, Quantitative study on catalysis of unpaired electrons in carbon edge sites, Carbon 210 (2023) 118069.

[58] W. Zhang, L. Zhou, H. Deng, Ag modified g-C_3N_4 composites with enhanced visible-light photocatalytic activity for diclofenac degradation, J. Mol. Catal. Chem. 423 (2016) 270–276.

[59] Y. Yang, Y. Gou, F. Liu, X. Yuan, Y. Guo, S. Zhang, W. Guo, M. Huo, Preparation and enhanced visible-light photocatalytic activity of silver deposited graphitic carbon nitride plasmonic photocatalyst, Appl. Catal., B 142–143 (2013) 828–837.

[60] Y. Bu, Z. Chen, W. Li, Using electrochemical methods to study the promotion mechanism of the photoelectric conversion performance of Ag-modified mesoporous g-C_3N_4 heterojunction material, Appl. Catal., B 144 (2014) 622–630.

[61] G. Kresse, J. Hafner, Ab-initio molecular-dynamics for open-shell transition-metals, Phys. Rev. B 48 (1993) 13115–13118.

[62] G. Kresse, J. Furthmuller, Efficient iterative schemes for ab initio total-energy calculations using a plane-wave basis set, Phys. Rev. B 54 (1996) 11169–11186.

[63] J.P. Perdew, K. Burke, Y. Wang, Generalized gradient approximation for the exchange-correlation hole of a many-electron system, Phys. Rev. B 54 (1996) 16533–16539.

[64] P.E. Blochl, Projector augmented-wave method, Phys. Rev. B 50 (1994) 17953–17979.

[65] G. Kresse, D. Joubert, From ultrasoft pseudopotentials to the projector augmented-wave method, Phys. Rev. B 59 (1999) 1758–1775.

[66] S. Grimme, J. Antony, S. Ehrlich, H. Krieg, A consistent and accurate ab initio parametrization of density functional dispersion correction (DFT-D) for the 94 elements H-Pu, J. Chem. Phys. 132 (2010) 154104.

[67] M.J. Frisch, G.W. Trucks, H.B. Schlegel, G.E. Scuseria, M.A. Robb, J. R. Cheeseman, G. Scalmani, V. Barone, G.A. Petersson, H. Nakatsuji, X. Li, M. Caricato, A.V. Marenich, J. Bloino, B.G. Janesko, R. Gomperts, B. Mennucci, H. P. Hratchian, J.V. Ortiz, A.F. Izmaylov, J.L. Sonnenberg, D. Williams-Young, F. Ding, F. Lipparini, F. Egidi, J. Goings, B. Peng, A. Petrone, T. Henderson, D. Ranasinghe, V.G. Zakrzewski, J. Gao, N. Rega, G. Zheng, W. Liang, M. Hada, M. Ehara, K. Toyota, R. Fukuda, J. Hasegawa, M. Ishida, T. Nakajima, Y. Honda, O. Kitao, H. Nakai, T. Vreven, K. Throssell, J.A. Montgomery Jr., J.E. Peralta, F. Ogliaro, M.J. Bearpark, J.J. Heyd, E.N. Brothers, K.N. Kudin, V.N. Staroverov, T.A. Keith, R. Kobayashi, J. Normand, K. Raghavachari, A.P. Rendell, J.C. Burant, S.S. Iyengar, J. Tomasi, M. Cossi, J.M. Millam, M. Klene, C. Adamo, R. Cammi, J. W. Ochterski, R.L. Martin, K. Morokuma, O. Farkas, J.B. Foresman, D.J. Fox, Gaussian 16, Revision B.01, Gaussian Inc., Wallingford (CT), 2016.

[68] A.D. Becke, Density–functional thermochemistry. III. The role of exact exchange, J. Chem. Phys. 98 (1993) 5648–5652.

[69] J.S. Binkley, J.A. Pople, W.J. Hehre, Self-consistent molecular orbital methods. 21. Small split-valence basis sets for first-row elements, J. Am. Chem. Soc. 102 (1980) 939–947.

[70] E. Runge, E.K.U. Gross, Density-functional theory for time-dependent systems, Phys. Rev. Lett. 52 (1984) 997–1000.

[71] A. Cousson, B. Nicolai, F. Fillauxc, Melamine (1,3,5-triazine-2,4,6-triamine): a neutron diffraction study at 14 K, Acta Crystallogr. E61 (2005) o222–o224.

[72] B.V. Lotsch, W. Schnic, New light on an old story: formation of melam during thermal condensation of melamine, Chem. Eur J. 13 (2007) 4956–4968.

[73] T. Tyborski, C. Merschjann, S. Orthmann, F. Yang, M.-C. Lux-Steiner, T. Schedel-Niedrig, Crystal structure of polymeric carbon nitride and the determination of its process-temperature-induced modifications, J. Condens. Matter Phys. 25 (2013) 395402, 1–395402–7.

[74] N. Liu, T. Li, Z. Zhao, J. Liu, X. Luo, X. Yuan, K. Luo, J. He, D. Yu, Y. Zhao, From triazine to heptazine: Origin of graphitic carbon nitride as a photocatalyst, ACS Omega 5 (2020) 12557–12567.

[75] K. Akaike, K. Aoyama, S. Dekubo, A. Onishi, K. Kanai, Characterizing electronic structure near the energy gap of graphitic carbon nitride based on rational interpretation of chemical analysis, Chem. Mater. 30 (2018) 2341–2352.

[76] F. Fina, S.K. Callear, G.M. Carins, J.T.S. Irvine, Structural investigation of graphitic carbon nitride via XRD and Neutron Diffraction, Chem. Mater. 27 (2015) 2612–2618.

[77] V.W. Lau, M.B. Mesch, V. Duppel, V. Blum, J. Senker, B.V. Lotsch, Low molecular-weight carbon nitrides for solar hydrogen evolution, J. Am. Chem. Soc. 137 (2015) 1064–1072.

[78] Q. Wang, S. Guan, B. Li, 2D graphitic-C_3N_4 hybridized with 1D flux-grown Na-modified $K_2Ti_6O_{13}$ nanobelts for enhanced simulated sunlight and visible-light photocatalytic performance, Catal. Sci. Technol. 7 (2017) 4064.

[79] C. Zhang, J. Liu, X. Huang, D. Chen, S. Xu, Multistage polymerization design for g-C_3N_4 nanosheets with enhanced photocatalytic activity by modifying the polymerization process of melamine, ACS Omega 4 (2019) 17148–17159.

[80] B. Zhang, Q. Wang, J. Zhuang, S. Guan, B. Li, Molten salt assisted in-situ synthesis of TiO_2/g-C_3N_4 composites with enhanced visible-light-driven photocatalytic activity and adsorption ability, J. Photochem. Photobiol. A 362 (2018) 1–13.

[81] S.C. Yan, Z.S. Li, Z.G. Zou, Photodegradation performance of g-C_3N_4 fabricated by directly heating melamine, Langmuir 25 (2009) 10397–10401.

[82] Y.C. Zhao, Z. Liu, W.G. Chu, L. Song, Z.X. Zhang, D.L. Yu, Y.J. Tian, S.S. Xie, L. F. Sun, Large-scale synthesis of nitrogen-rich carbon nitride microfibers by using graphitic carbon nitride as precursor, J. Adv. Mater. 20 (2008) 1777–1781.

[83] R. Vijayarangan, M. Sakar, R. Ilangovan, Stabilization of melon phase during the formation of g-C_3N_4 from melamine and its structure-property relationship towards photocatalytic degradation of dyes under sunlight, J. Mater. Sci. Mater. Electron. 33 (2022) 9057–9065.

[84] X. Song, Q. Yang, X. Jiang, M. Yin, L. Zhou, Porous graphitic carbon nitride nanosheets prepared under self-producing atmosphere for highly improved photocatalytic activity, Appl. Catal. B Environ. 217 (2017) 322–330.
[85] W. Zhang, C. Xu, T. Kobayashi, Y. Zhong, Z. Guo, H. Zhan, M. Pruski, W. Huang, Hydrazone-linked heptazine polymeric carbon nitrides for synergistic visible-light-driven catalysis, Chemistry 26 (2020) 7358–7364.
[86] P. Praus, L. Svoboda, M. Ritz, I. Troppova, M. Sihor, K. Koci, Graphitic carbon nitride: synthesis, characterization and photocatalytic decomposition of nitrous oxide, Mater. Chem. Phys. 193 (2017) 438, 436.
[87] Y. Chen, B. Wang, S. Lin, Y. Zhang, X. Wang, Activation of n → π* transitions in two-dimensional conjugated polymers for visible light photocatalysis, J. Phys. Chem. C 118 (2014) 29981–29989.
[88] W.J. Ong, L.L. Tan, S.P. Chai, S.T. Yong, Graphene oxide as a structure-directing agent for the two-dimensional interface engineering of sandwich-like graphene–g-C_3N_4 hybrid nanostructures with enhanced visible-light photoreduction of CO_2 to methane, Chem. Commun. 51 (2015) 858–861.
[89] H. Wang, X. Sun, D. Li, X. Zhang, S. Chen, W. Shao, Y. Tian, Y. Xie, Boosting hot-electron generation: exciton dissociation at the order–disorder interfaces in polymeric photocatalysts, J. Am. Chem. Soc. 139 (2017) 2468–2473.
[90] G. Zhang, M. Liu, T. Heil, S. Zafeiratos, A. Savateev, M. Antonietti, X. Wang, Electron deficient monomers that optimize nucleation and enhance the photocatalytic redox activity of carbon nitrides, Angew. Chem. Int. Ed. 58 (2019) 14950–14954.
[91] R.-S. Juang, S.-H. Lin, P.-Y. Hsueh, Removal of binary azo dyes from water by UV-irradiated degradation in TiO_2 suspensions, J. Hazard Mater. 182 (2010) 820–826.
[92] S. Malato, P. Fernandez-Ibanez, M.I. Maldonado, J. Blanco, W. Gernjak, Decontamination and disinfection of water by solar photocatalysis: recent overview and trends, Catal. Today 147 (2009) 1–59.
[93] A. Priya, R.A. Senthil, A. Selvi, P. Arunachalam, C.K.S. Kumar, J. Madhavan, R. Boddula, R. Pothu, A.M. Al-Mayouf, A study of photocatalytic and photoelectrochemical activity of as-synthesized WO_3/g-C_3N_4 composite photocatalysts for AO7 degradation, Mater. Sci. Energy Technol. 3 (2020) 43–50.
[94] J.J. He, H.Q. Sun, S. Indrawirawan, X.G. Duan, M.O. Tade, S.B. Wang, J.J. He, H. Q. Sun, S. Indrawirawan, X.G. Duan, M.O. Tade, S.B. Wang, Novel poly-oxometalate@g-C_3N_4 hybrid photocatalysts for degradation of dyes and phenolics, J. Colloid Interface Sci. 456 (2015) 15–21.
[95] X.S. Rong, F.X. Qiu, J. Rong, J. Yan, H. Zhao, X.L. Zhu, D.Y. Yang, Synthesis of porous g- C_3N_4/La and enhanced photocatalytic activity for the degradation of phenol under visible light irradiation, J. Solid State Chem. 230 (2015) 126–134.
[96] M. Xiong, L. Chen, Q. Yuan, J. He, S.L. Luo, C.T. Au, S.F. Yin, Controlled synthesis of graphitic carbon nitride/beta bismuth oxide composite and its high visible-light photocatalytic activity, Carbon 86 (2015) 217–224.
[97] S.-M. Lam, J.-C. Sin, A.R. Mohamed, A review on photocatalytic application of g-C_3N_4/semiconductor (CNS) nanocomposites towards the erasure of dyeing wastewater – review, Mater. Sci. Semicond. Process. 47 (2016) 62–84.
[98] J.Q. Ma, Q.F. Yang, Y.Z. Wen, W.P. Liu, Fe-g-C_3N_4/graphitized mesoporous carbon composite as an effective Fenton-like catalyst in a wide pH range, Appl. Catal. B Environ. 201 (2017) 232–240.
[99] H. Chakhtouna, H. Benzeid, N. Zari, A.E.K. Qaiss, R. Bouhfid, Recent progress on Ag/TiO_2 photocatalysts: photocatalytic and bactericidal behaviors, Environ. Sci. Pollut. Res. 28 (2021) 44638–54466.
[100] H. Lan, L. Li, H. Liu, X. An, F. Liu, C. Chen, J. Qu, Melem-based derivatives as metal-free photocatalysts for simultaneous reduction of Cr(VI) and degradation of 5-Sulfosalicylic acid, J. Colloid Interface Sci. 507 (2017) 162–171.
[101] Q. Zhang, Y. Xiao, L. Yang, Y. Wen, Z. Xiong, L. Lei, L. Wang, Q. Zeng, Branched core-shell a-TiO_2@N-TiO_2 nanospheres with gradient-doped N for highly efficient photocatalytic applications, Chin. Chem. Lett. 34 (2023) 107628.
[102] A. Beyhaqi, S. Mohammad T. Azimi, Z. Chen, C. Hu, Q. Zeng, Exfoliated and plicated g-C_3N_4 nanosheets for efficient photocatalytic organic degradation and hydrogen evolution, Int. J. Hydrogen Energy 46 (2021) 20547–20559.